ADVANCED INTELLIGENT SYSTEMS Open Access
www.advintellsyst.com

Remote Propulsion of Miniaturized Mechanical Devices via Infrared-Irradiated Reversible Shape Memory Polymers

*Yacov Carmiel, Avraham Israel Bram, Nurit Atar, Asaf Bolker, Noam Eliaz, Nehora Moshe, Shiran Barmoha, Adva Bouzaglou, Ehud Galun, Irina Gouzman, and Ronen Verker**

Remote propulsion of miniature mechanical devices possesses a great challenge to the scientific community. Herein, a lightweight two-way shape memory polymer (2WSMP)-based motor is presented, which operates a demo vehicle via a novel infrared-irradiated 2WSMP actuator. Most of the polymers that possess 2WSMP properties suffer from inadequate mechanical properties and low durability in harsh environments. Herein, the 2WSMP bilayer actuator, based on Kapton and polyPOSS (PP), possesses superior 2WSMP and mechanical properties, high lifting abilities, and durability in harsh environments. Kapton is well known for its outstanding physical properties. PP, a polyhedral oligomeric silsesquioxane (POSS)-based epoxy-like thermoset, possesses unique properties. Its advanced ability to maintain mechanical properties over a range of temperatures, while presenting a constant coefficient of thermal expansion, is essential for its 2WSMP actuation properties. The effects of the Kapton and PP layers' thickness on the force and deflection, generated by the 2WSMP actuators during heating, are studied. A theoretical model is used to predict the actuator's deflection, based on the layers' thickness. These actuators present excellent thermal stability at temperatures as high as 150 °C, while maintaining outstanding motion repeatability and extremely high lifting capacity of up to 6500 times of their own weight.

1. Introduction

Shape memory is the ability of a material to return to a preprogrammed shape after it has been deformed by an external force. Shape memory polymer actuators have gained interest due to their high stress-to-weight ratio and their responsiveness to a wide variety of external stimuli.[1] Remote activation of the actuators is essential for applications where an internal power source is unavailable. Irradiation in the vis–IR range, preferably by a laser beam, is the most common way to activate actuators, as it enables long distances between the irradiation source and the actuator.[2] There are two main mechanisms for irradiation-based actuators: photochemical and photothermal. For a photochemical activation, the polymer itself contains reactive groups that react when exposed to light of a suitable wavelength, thus altering the structure of the polymer. The structural change leads to a change in dimensions and the shape of the actuator.[3–12] Photothermal actuation is based on the conversion of light to heat, leading to a heat-induced shape memory effect (SME). This can be achieved either by incorporation of light-absorbing additives or using light at a wavelength effectively absorbed by the polymer itself.[2,13–16]

Polymers that can only recover their original shape are referred to as one-way shape memory polymers (1WSMP); they have been thoroughly studied since the late 1980s.[17–28] Polymers that can change back and forth between two shapes are referred to as two-way shape memory polymers (2WSMPs). The ability of polymers to revert between two or more shapes has gained great interest in recent years.

Y. Carmiel, A. I. Bram, N. Atar, A. Bolker, N. Moshe, S. Barmoha, A. Bouzaglou, I. Gouzman, R. Verker
Space Environment Department
Soreq Nuclear Research Center
Yavne 81800, Israel
E-mail: rverker@soreq.gov.il

The ORCID identification number(s) for the author(s) of this article can be found under https://doi.org/10.1002/aisy.202200006.

DOI: 10.1002/aisy.202200006

A. I. Bram
Licensing & Safety Office
Israel Atomic Energy Commission
P.O. Box 7061, Tel Aviv, Israel

A. I. Bram, N. Eliaz
Department of Materials Science and Engineering
Tel-Aviv University
Ramat Aviv, Tel Aviv 6997801, Israel

E. Galun
Directorate of Defense Research and Development
Israel Ministry of Defense
Tel-Aviv 61909, Israel

The first reported 2WSMPs were based on semicrystalline polymers with a stretch-induced crystallization (SIC) effect. However, this effect required a constant load on the polymer to achieve reversible shape change.[29–37] To overcome the need for constant load, two approaches were developed. The first approach uses polymers with crystalline segments that melt within a wide temperature range. The reversible shape change is achieved in this case by heating the material to a temperature at which only some of the crystalline segments melt and others remain crystalline. During cooling, the remaining crystals direct crystallization in the desired direction back to the programmed shape.[38–42] The second approach is based on combining two types of crystalline segments by crosslinking together two polymers with distinguishable melting temperatures (T_m). Heating and cooling around the lower T_m activate the 2WSMP functions.[43–46] The downside of these approaches is that if the actuator exceeds its working temperature and becomes fully amorphous, it loses its mechanical properties and related functionality. To overcome the temperature limitations of the T_m mechanism, 2WSMPs are combined with elastomers. Upon heating, the 2WSMP contracts toward its original shape due to crystal melting, thus applying stress on the elastomer. When cooled, the elastomer applies the same stress on the 2WSMP, leading the crystals' growth back to the deformed shape. The combination can be as separate layers[47–50] or at the molecular level to form an interpenetrating network (IPN).[51]

In contrast to the crystal melting mechanisms, 2WSMP actuators can be prepared by joining two polymers, where one polymer undergoes a high volumetric change in response to an external stimulus such as heat or light.[52–54] These actuators are commonly based on the difference in the coefficient of thermal expansion (CTE) of the polymers, similar to bimetal devices. During heating, the layer with a higher CTE (i.e., the active layer) expands more than the passive layer, which leads to bending of the actuator.[55] The actuators can also be designed to bend in the opposite direction when cooled below ambient temperature.[56] To maximize the bending effect, the CTE difference between the layers should be as high as possible. Carbon nanotubes (CNTs) or graphene are often used as the passive layer, due to their low CTE. Polydimethylsiloxane (PDMS) and various polyolefins are commonly used as the active layer due to their high CTE.[57–60]

The force generated by a 2WSMP affects its potential application. A common method to normalize and compare the force generated by various 2WSMPs of different dimensions and densities is to normalize the force generated by the actuator by its weight. Another method is simply to compare the stress generated by various 2WSMPs.

Qi et al. produced a semicrystallized ethylene-vinyl acetate (EVA) copolymer fiber with a two-way SME and found that a single EVA fiber could lift more than 143 times its own weight.[61] Wang et al. produced light-actuated 2WSMP by incorporating polydopamine (PDA) nanospheres into semicrystalline polymer networks. This 2WSMP lifted 3541 times its own weight while generating 1.1 MPa stress.[62] Yang et al. presented a near-IR light-stimulated actuator with fully reversible lifting motions, which could lift 11,200 times its own weight.[63] Lu et al. reported an interpenetrating material that can reversibly shrink and expand under thermal stimulus at a maximum temperature of 140 °C.[64] The actuation stress of this material is 2.53 MPa and it can lift 30,000 times its own weight. For comparison, the actuation stress of a human skeletal muscle is 0.35 MPa.[64]

All of the aforementioned forces and stresses, however, were measured linearly in the direction of contraction. When forces and stresses were measured during bending of the actuators, the reported values were a few orders of magnitude lower. For example, the actuator of Zeng et al. was reported to have a lifting ability of 4.2 times its own weight,[58] that of Chen et al. lifted seven times its own weight,[59] and that of Li et al. lifted 27 times its own weight.[60] Chen et al. constructed graphene oxide/poly(*N*-isopropylacrylamide) hybrid film bilayer actuators, which display reversible bending–straightening behaviors in response to repeated cycles of near-IR light irradiation.[65] A maximal 10 MPa stress was measured, but with a slow actuation rate of several minutes per cycle.

Although the above materials, used for 2WSMP actuators, demonstrate a wide motion range and the ability to form complex shapes, they lack durability to extreme conditions, such as elevated temperatures, and have limited lifting ability during bending. Currently, 2WSMP actuators suffer severe loss of mechanical properties at elevated temperatures. Furthermore, environmental effects such as ionizing radiation and corrosive environment can also damage most polymers used for 2WSMPs by degradation of mechanical properties and etching.

Here, we present unique 2WSMP bilayer actuators based on polyimide (Kapton) and polyPOSS (PP), a novel nanocomposite with high durability to extreme conditions.[66] The goal of this research is to study the effect of the Kapton and PP layers' thickness on the reversible SME, deflection, and forces that the 2WSMP actuators can produce.

The 2WSMP actuators present excellent thermal stability at temperatures as high as 150 °C, while maintaining outstanding motion repeatability and extremely high lifting capacity of up to 6500 times of their own weight. Moreover, they can be remotely activated by IR irradiation, which makes them highly suitable for remote operation of tiny devices. Here, we demonstrate these features of the new material by integrating these actuators in a miniature engine and vehicle. These machines prove that these actuators can be used as remotely activated, lightweight driving mechanisms.

2. Experimental Section

2.1. Materials

EP0409 glycidyl polyhedral oligomeric silsesquioxane (POSS) was purchased from Hybrid Plastics, USA. Jeffamine D-230 poly(propylene glycol)bis(2-aminopropyl ether) curing agent was purchased from Huntsman, The Netherlands. Pristine Kapton HN polyimide films were purchased from Dupont, USA. Polybismaleimide (BMI)-689 resin was obtained from Designer Molecules, USA.

2.2. 2WSMP Actuators

EP0409 and Jeffamine D-230 were preheated to 80 °C and mixed at a 2.8:1 POSS:Jeffamine weight ratio to form the polyPOSS

(PP).[67] Pristine Kapton (PK) films with a thickness of either 50 or 125 μm and lateral dimensions of 2.5 × 5.5 cm^2 were used as substrates. Kapton tape was placed on the edge of the films to form molds with depths of 60, 120, or 180 μm. The Kapton molds were treated by air radio frequency (RF) plasma cleaner (PDC-3XG, Harrick Plasma) for 2 h. The precured PP was poured into the molds and cured at 100 °C for 1.5 h, followed by postcuring at 130 °C for 3 h. After curing, the mold spontaneously adopted a curved shape. The Kapton tape was removed, and the 2.5 × 5.5 cm^2 substrate was cut to form actuators with general dimensions of 1 × 2.5 cm^2 and PP layer dimensions of 1 × 1.5 cm^2. **Figure 1** illustrates the actuator production process. Each actuator was named according to the thicknesses of the PK and PP layers, as listed in **Table 1**.

Table 1. List of 2WSMP actuators.

Actuator acronym	PK thickness [μm]	PP thickness [μm]
PK50–PP60	50	60
PK50–PP120	50	120
PK50–PP180	50	180
PK125–PP60	125	60
PK125–PP120	125	120
PK125–PP180	125	180

2.3. Characterization and Analysis Techniques

Dynamic mechanical analyzer (DMA) (Q800, TA Instruments) was used to characterize the mechanical and thermomechanical properties of the pristine materials (PP and PK) and actuators. All measurements were performed using a three-point bending clamp in nitrogen environment. Young's modulus measurements of PP and PK were performed using the strain rate mode. The PK samples size was 10 × 7 × 0.125 mm^3, and the PP samples size was 20 × 3 × 0.5 mm^3. The measurements were performed using a support span of 5 mm, a preload of 0.05 N, and a strain rate of 0.5% min^{-1} up to a final strain of 0.5%. These measurements were performed at temperatures between 30 and 150 °C, at increments of 10 °C. Each measurement was repeated three times.

Static force versus temperature measurements of the actuators were performed using the strain rate mode, a preload of 5 mN, and a support span of 5 mm. The actuators were placed on the supports with their concave side facing upward and were heated to 150 °C at a rate of 2 °C min^{-1}. Each measurement was repeated three times. The actuators were then cooled back to 22 °C at a rate of 3 °C min^{-1}.

Inverse deflection versus temperature measurements of the actuators were performed using the controlled force mode, a preload of 5 mN, and a support span of 5 mm. The actuators were placed on the supports with their concave side facing upward and were heated to 150 °C at a rate of 5 °C min^{-1}. The actuators were equilibrated for 10 min at that temperature and then were cooled

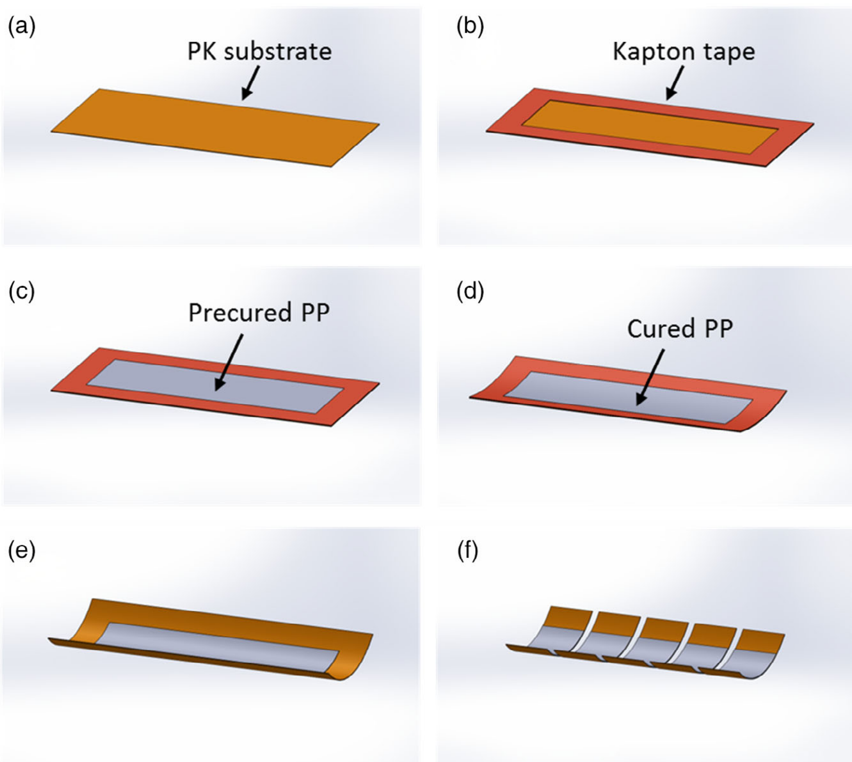

Figure 1. 2WSMP actuators' production process: a) A PK film is used as a substrate. b) A Kapton tape is placed on the edge of the film to form a mold. c) Precured PP is poured into the mold. d) The PP is cured. e) The Kapton tape is removed. f) Actuators are cut from the substrate.

back to 30 °C at the same rate. Ten heating/cooling cycles were performed for each measurement.

Optical absorbance and transmittance measurements were performed using a spectrophotometer (V-570, Jasco). These measurements were conducted between 350 and 1000 nm, at a scanning speed of 200 nm min^{-1}.

CTE measurements were performed using a thermomechanical analyzer (TMA PT 1600, Linseis GMBH), operated in the push-rod dilatometer mode, with alumina sample holder and piston. Three samples of each material were measured. The measured polymer samples were shaped as rods with a diameter of 4.65 mm and a length of 20 mm. The samples were heated at a rate of 2 °C min^{-1} in helium environment. The change in sample length was measured by the deflection of the piston.

Calorimetric investigation of fully cured PP samples was carried out using differential scanning calorimetry (DSC), 1 STARe system (Mettler Toledo, Inc.). The samples for DSC were weighed on Sartorius SE2 microbalance with precision of ±0.1 µg and their net weight was set between 40 and 95 mg. The samples were placed in aluminum crucibles. The DSC measurements were done in nitrogen environment while heating at a rate of 10 °C min^{-1}.

D8 discover X-ray diffractometer (Bruker, Inc.) was used to assess the crystallographic structure of the PP. The measurements were performed using a Cu tube with a wavelength of 1.54 Å. The scan started at $2\theta = 5°$, with 2θ increments of 0.02° at a rate of 1 increment per second. A fully cured PP sample, having a size of $25 \times 25 \times 3\ mm^3$, was placed on a ceramic plate equipped with a heating pad (HK5318, Minco) and secured with Kapton tape. The diffraction patterns were acquired both at room temperature (RT) and at 130 °C.

The actuators' internal stress and deformation were simulated using the solid mechanics module of the ABAQUS finite-element analysis (FEA) software. The empirical expressions, used for the temperature-dependent Young's modulus of the PP and PK materials, were derived by performing a functional fit to the measured data using the CurveExpert software.

2.4. Processes

The actuators were remotely heated for shape memory tests using an IR source working at a continuous spectrum of 350–1000 nm, a peak wavelength of 860 nm, and a radiative power of 450 mW cm^{-2}, at 15 cm distance between the actuator and the source.

2WSMP-based mechanisms were prepared from Kapton and 3D-printed BMI. Kapton parts were manufactured from the 125 µm-thick Kapton film. Kapton was thermoformed at 435 °C for 8 h under nitrogen flow to yield a flat and dark Kapton film.[68] BMI parts were printed by a commercial 3D printer (Max Mini UV 385 nm, ASIGA) using a custom-made ink.[69]

3. Results and Discussion

Heating the actuators caused them to unbend, reaching a fully straight form at 130 °C and above. **Figure 2**a shows a PK125-PP180 actuator at both bend and straight shapes. The shape change is bidirectional, and the actuator returns to its curved shape once cooled.

3.1. PP Characterization

One of the main mechanisms behind many SMPs is a crystalline to amorphous phase change or glassy- to rubbery-state transition. As Kapton has no known phase transitions within the 30–150 °C temperature range,[70] we performed measurements on the PP to determine whether it has one. The structure of PP was characterized by X-ray diffraction (XRD), both at RT and at 130 °C. The diffraction patterns indicated an almost entirely amorphous material, with a small peak at 8°, which corresponds to aggregates of the POSS component.[71–73] There were no significant changes in the diffraction pattern when heated, other than those associated with thermal expansion; the peak at 8° also remained unchanged (Figure S1, Supporting Information). DSC measurements did not show any phase transition of the PP within the 30–130 °C temperature range (Figure S2, Supporting Information). These results indicate that phase change is not involved in the shape change of these actuators. Therefore, the main cause can be attributed to the variance in the thermal expansion of the PP and PK layers. As the thermal expansion of PK is well documented as 17 ppm K^{-1},[70] the PP thermal expansion was measured, as it plays an important role in this study. The PP showed a uniform expansion within the 25–135 °C temperature range, with an average CTE of 162 ppm K^{-1} (Figure S3, Supporting Information). Due to the order of magnitude difference in the CTE, the PP will be addressed as the active layer and the PK as the passive layer. The validation of the thermal expansion mismatch as the driving force for the reversible shape change will be further discussed in the following sections.

3.2. Deflection and Force Measurements

The deflection of the actuators during thermal cycles was measured by DMA. To visualize the repeatability of the deflection measurements, Figure 2b shows the results of the deflection measurements during ten temperature cycles, from 30 to 150 °C, for PK125-PP180 actuator. The various actuators were also exposed to 105 thermal cycles between 25 and 150 °C using a hot plate. These actuators showed no sign of fatigue or failure during this exposure, as was shown by the full transition from a bent state at 25 °C to a straight state at 150 °C during all cycles (Figure S4 and Video S1, Supporting Information). Video S1, Supporting Information, presents the full motion of the actuators at the last thermal cycle. Figure 2c presents the deflection at 150 °C versus the PP thickness of the various actuators. The maximal deflection (630 µm) was measured for the PK50–PP60 actuator, while the smallest deflection (140 µm) was measured for the PK125–PP60 actuator. For both types of actuators having PK thickness of either 50 or 125 µm, as the thickness of the PP layer increased, the trend of the deflection values seemed to converge. For actuators with PK thickness of 50 µm, increasing the PP thickness caused the deflection to decrease from 630 to 400 µm, while for actuators with PK thickness of 125 µm, the deflection increased from 140 to 240 µm. It appears that for a given PK thickness and temperature, the

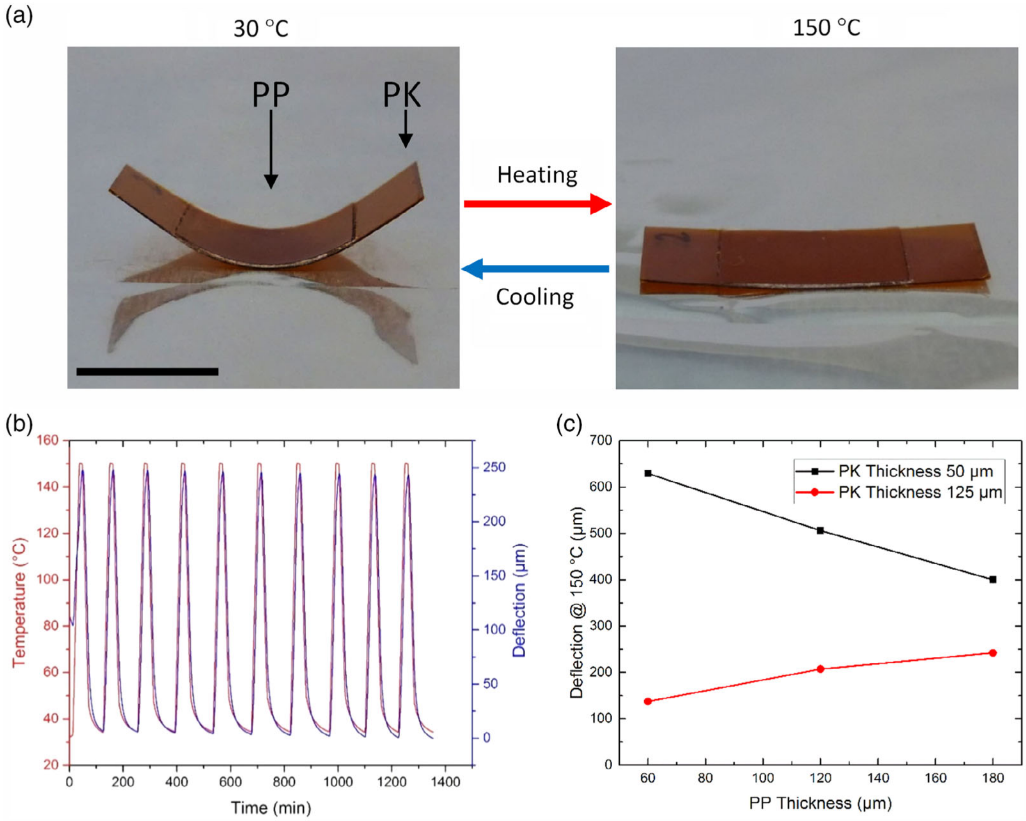

Figure 2. a) Temperature-induced shape change of a PK125–PP180 actuator. Scale bar: 1 cm. b) Temperature and deflection versus time measurements during ten temperature cycles of a PK125–PP180 actuator. c) Deflection of the actuators at 150 °C. The error bars are smaller than ±3 μm.

governing parameter for determining the deflection is the PP thickness.

Figure 3a presents the static force produced by 2WSMP actuators at a given temperature. The general trend of the increase in the static force as a function of temperature is almost linear for most of the actuators. For some of the actuators, the increase in the static force can be divided into two parts: a slow increase up to a temperature of 70–90 °C, followed by a fast increase up to 150 °C. Figure 3b shows the static force values generated by the actuators at 147 °C versus the actuator type (i.e., the layer thickness). The inset shows the direction of the measured force in the three-point bending mode. An almost linear relationship can be noticed between the static force and the PP layer thickness, for a given PK layer thickness. PK50–PP60 produced the smallest static force values, while PK125–PP180 produced the highest values. In general, it can be noticed that increasing the thickness of either the PK layer or the PP layer increases the generated static force.

Each measurement started with the actuator at ambient temperature, at which it is in a curved shape, driven by the

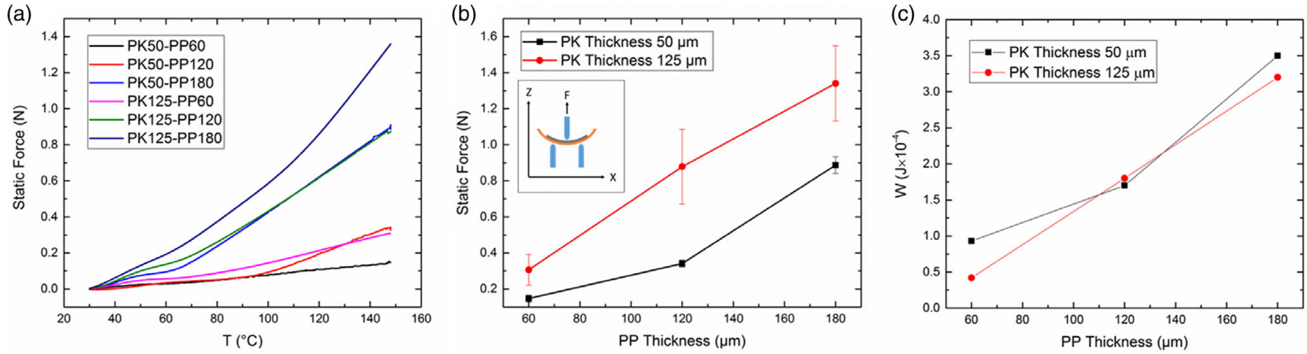

Figure 3. a) The static force produced by the actuators as a function of temperature. b) Static force values as a function of the PP thickness at 147 °C. The inset shows the direction of the measured force. c) Maximal theoretical work values versus PP layer thickness for the various PK–PP 2WSMP actuators.

contraction of the PP layer. The curvature depends on the force applied by the PP layer and by the thickness of the PK layer. As the force applied by the PP layer is proportional to its thickness (for a given width), the main parameters that govern the curvature of the actuators are the thickness of both layers. In extreme cases in which one layer is thick and the other is thin, there will be no curving. For example, if the PP layer is extremely thin in comparison with the thickness of the PK layer, the contraction force it can apply is too small to bend the PK layer. If the PK layer is extremely thin in comparison with the thickness of the PP layer, the force it can apply to resist contraction will be negligible and the PP layer will contract linearly along the *X*-axis without bending (see the inset of Figure 3b). For intermediate cases, the curvature is determined by the layer's thickness ratio and by the total thickness of the actuator; see a detailed discussion in Section 3.4.[74]

During the static force measurement, once heated, the actuator is forced to stay in its original curved shape by the three-point bending fixture. The static force is measured in the *Z*-direction, as shown in the inset of Figure 3b. The measured static force is equivalent to the force needed to bend the actuator to this curvature at 147 °C. As the force required to bend a material depends on its thickness, increasing the thickness of either the PP or the PK layer results in an increase in the static force.

For example, the measured static force of the PK50–PP60 actuator was ≈0.15 N. Increasing the thickness of the PK layer to 125 μm (PK125–PP60) or the PP thickness to 120 μm (PK50–PP120) increased the static force to ≈0.3 N. Increasing the thickness of one of the layers of the PK50–PP120 actuator, to form actuator PK125–PP120 or PK50–PP180, increased the static force to ≈0.9 N.

These results exemplify a tradeoff between the thickness of the passive PK layer and the thickness of the active PP layer. That is, a 60 μm increase in the thickness of the PP layer is equivalent to increasing the PK layer thickness by 75 μm to yield similar static force.

The 2WSMP bilayer actuators can produce static forces as high as 0.9 N in the case of PK50–PP180 and 1.3 N in the case of PK125–PP180. The weight of the measured segment was 14.6 mg for the PK50–PP180 actuator and 19.9 mg for the PK125–PP180 actuator. This leads to effective force-to-weight ratios of 61:1 and 65:1 N g^{-1}, respectively, equivalent to an actuator lifting capacity of up to 6500 times its weight.

The maximal theoretical work (W_m) at the center point of the various 2WSMP actuators was calculated according to Equation (1)

$$W_m = F_s \cdot D \tag{1}$$

where F_s is the static force and D is the deflection. The center point of each actuator experiences the highest deflection. **Table 2** summarizes the PK–PP actuators' maximal deflection and static force. These values were used in the calculation of the maximal work that each type of actuator can produce. Figure 3c presents the work values versus the PP layer thickness for the various PK–PP 2WSMP actuators. For actuators with a PK thickness of 125 μm, the attained work values increase linearly with the PP layer thickness. Interestingly, for the actuators with PK thickness of 50 μm, the attained work values also increase with the PP layer thickness, even though at the same time the deflection monotonically decreases, as shown in Figure 2c. The similarity in the work values of the PK50 and PK125 actuators indicates that the work depends solely on the PP layer thickness, mainly due to an increase in the static force. In the case of a decrease in the deflection, shown in Figure 2c, the high increase of the static force compensates for this decrease, and the end result is a monotonic increase in the product of the deflection and force. These results match well to our definition of the PP layer as the active layer.

Table 2. Summary of the PK–PP actuators' maximal deflection and static force.

Actuator acronym	Maximal deflection [μm]	Maximal force [N]
PK50–PP60	629	0.147
PK50–PP120	506	0.341
PK50–PP180	400	0.887
PK125–PP60	137	0.306
PK125–PP120	207	0.878
PK125–PP180	242	1.341

3.3. SME Response Time Measurements

An important parameter for actuators is the SME time (t_{SME}), that is, the time between the introduction of a stimulus and the resulting shape change. The actuators' response time was measured during heating by the IR source at a 15 cm distance, as well as during cooling under ambient conditions. The results are presented in **Table 3**; each actuator was measured 4 times. For all actuators, t_{SME} during heating was between 10 and 16 s and between 10 and 19 s during cooling. For a given PK thickness, t_{SME} increased as the thickness of the PP layer increased. Increasing the PK thickness from 50 to 125 μm had a smaller effect on t_{SME}, indicating that the heating and cooling rate of the PP layer is the governing factor. In addition to the PP mass, another factor that governs t_{SME} is the optical absorbance of the actuators. Typical optical absorbance and transmittance spectra of the actuators can be found in Figure S5 (Supporting Information).

Table 3. Average time for the SME (t_{SME}) during heating and cooling of the actuators.

Actuator acronym	t_{SME} during heating [s]	t_{SME} during cooling [s]
PK50–PP60	11 ± 1	12 ± 1
PK50–PP120	12 ± 1	15 ± 1
PK50–PP180	14 ± 1	15 ± 1
PK125–PP60	10 ± 1	10 ± 2
PK125–PP120	14 ± 1	15 ± 1
PK125–PP180	16 ± 1	19 ± 3

3.4. Theoretical Model and FEA

When two materials with different CTEs are bonded together, temperature changes will cause the structure to bend. This phenomenon has been studied by Stephen Timoshenko in 1925 for bimetal thermostats. Timoshenko formulated an equation that relates the beam curvature to the layers' thickness and thermomechanical properties.[74]

$$\frac{1}{\rho} = \frac{6(\alpha_2 - \alpha_1)(\Delta T)(1+m)^2}{h[3(1+m)^2 + (1+mn)(m^2 + \frac{1}{mn})]} \tag{2}$$

where ρ is the radius of curvature, $1/\rho$ is the curvature, α_i represents the coefficients of thermal expansion, h is the total laminate thickness, m is the thickness (t) ratio of the two layers, $m = t_1/t_2$, and n is the temperature-dependent moduli of elasticity (E) ratio: $n = E_1(T)/E_2(T)$.

Although this equation was developed for the analysis of bimetal thermostats, it has been used successfully also to predict the curvature of polymeric bilayers.[75,76] However, there are some limitations to this equation. First, it was developed for narrow strips of isotropic materials; therefore, in the case of anisotropic Kapton, it can only account for forces acting parallel to the bilayer primary (long) axis. To comply with this limitation, all actuators were cut in an identified direction of the PK film, resulting in actuators that bent without twisting.[77]

Second, this equation calculates the curvature using the modulus and CTE of each material. These parameters are not constant and change with the temperature. The CTE of PP was shown to be 162 ppm K^{-1} in the range of 25–135 °C (Figure S3, Supporting Information). In our calculations, we assumed that it remains the same up to 150 °C. For PK, we used the CTE values reported by the manufacturer: 17 ppm K^{-1} within the temperature range of 30–100 °C and 32 ppm K^{-1} within the temperature range of 100–200 °C.[70]

Young's modulus of the PK and PP was measured by DMA in the temperature range of 30–150 °C. The PK's modulus decreased almost linearly from ≈4250 MPa at 30 °C to ≈3360 MPa at 150 °C. The PP's modulus first decreased from ≈640 MPa at 30 °C to ≈270 MPa when heated to 60 °C and then remained almost constant upon further heating to 150 °C (Figure S6, Supporting Information). Using these values, we calculated the curvature of PP–PK bilayers of various thicknesses at each temperature. The predicted deflection for actuators on a 5 mm support span was then calculated from this curvature.

Figure 4 provides a comparison between the model's calculated deflection and the DMA-measured deflection, versus the temperature. Each graph plots the deflection during 10 DMA temperature cycles between 30 and 150 °C.

The overlaid deflection–temperature curves demonstrate the accurate repetition of the actuator's movement. A deflection accuracy of ±5–±25 μm over a deflection range of 140–650 μm is measured. This accuracy can also be noticed in the results given in Figure 2b, which show deflection–time measurements during ten temperature cycles. The repetition in the deflection movement of the various actuators shows no degradation, indicating good adhesion between the PP and the PK layers.

The hysteresis in the deflection temperature cycles is the result of variation in temperature between the DMA oven and the actuators. When the DMA oven reaches 150 °C, the actuators continue to deflect, as they still did not reach that temperature. During cooling, the opposite phenomena occur. The oven temperature start to decrease; however, there is a delay in the decrease of the temperature of the actuators and as a result there is also a delay in the change of the actuators' deflection. At the final stage of cooling, as the oven temperature reaches 50 °C, the cooling rate decreased to about 0.2 °C min^{-1}. At this low cooling rate, there is no hysteresis between the oven and the actuator temperature. For actuators PK50–PP60, PK125–PP60, PK125–PP120, and PK125–PP180, the Timoshenko model fits quite well the deflection measurements during the cooling phase. The model fits the cooling curve rather than the heating curve as it assumes zero curvature at 150 °C, which is the starting point of the cooling curve. However, for actuators PK50–PP120 and PK50–PP180, the model predicts lower deflections than those measured during cooling, although still higher than the values measured during heating. This may indicate that when the PP layer is significantly thicker than the PK layer, there are other effects that were not accounted for by the model. One such effect can be deviation in the thickness and uniformity of the PP layer, in comparison with the PP thickness that was used in the model.

The Timoshenko model can be used to calculate the predicted maximal deflection based on the PP-to-PK thickness ratio. The deflection was calculated for actuators at 150 °C in three-point bending mode on a 5 mm support span. **Figure 5**a shows the predicted deflection versus the PP-to-PK thickness ratio (dashed lines). The maximal deflection coincides with 1.1 PP/PK thickness ratio (designated by the dotted vertical line). According to the model, a PP/PK thickness ratio of 1.1 is the optimal ratio for achieving the maximal deflection for a given PK thickness. The results of the experimental deflection measurements at 150 °C are also presented in Figure 5a as symbols. These results fit well the model's prediction. The comparison between the measured and model values explains the effect described in Figure 2c, where the deflection of the PK50 actuators decreased with increasing PP thickness, while the deflection of the PK125 actuators increased. This is because the PP/PK thickness ratio of the PK50 actuators was above 1.1 to begin with, while the PP/PK ratio of the PK125 actuators was initially below 1.1, and then increased toward 1.1 ratio, which provides maximal deflection.

FEA of the thermal-induced stress and deflection of a PK50–PP60 actuator at 150 °C is presented in Figure 5b. Many types of constitutive models exist to accurately simulate various types of SMPs.[78] In the presented material system, the SME is induced due the mismatch between the CTE of the two materials comprising the bilayer actuator. As the difference between the Young's moduli of the active and the passive layers has a negligible effect on the radius of curvature of a bilayer,[74] a simple approximation was used to compute the deformation of the bilayer.[79] The layers were treated as linear elastic materials, and the standard isotropic linear elastic constitutive model was used. In addition, the elastic strain used was the difference between the total strain, which is computed from derivatives of the displacement field, and the thermal strain. A 2D calculation was performed on an actuator with a total length of 5 mm. Figure 5c shows a zoomed-in stress map of the 0.5 mm section at the center of the actuator. The upper layer is the PK layer, and the lower layer is the PP layer. The original curved state

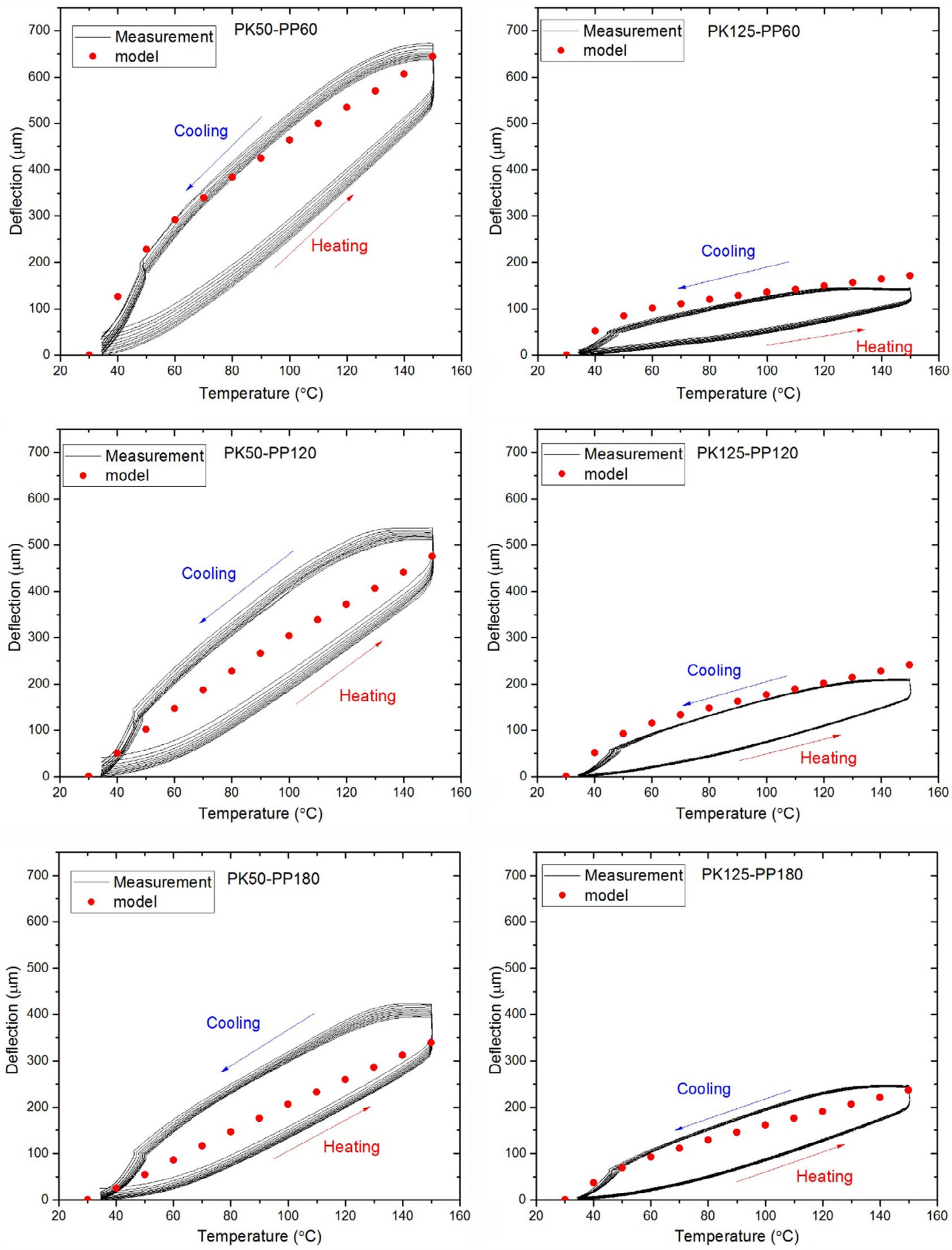

Figure 4. Comparison of the Timoshenko model calculated values and DMA measured values.

of the actuator at RT is marked by a black outline. The corresponding values to the colored stress field, depicted in the flat actuator, are shown on the color bar. The mechanical properties used to define each material are tabulated in Table S1, Supporting Information.

Two empirical expressions of the temperature-dependent Young's modulus were derived by performing a functional fit of the measured data (Figure S6, Supporting Information). Equation (3) was used for the PK temperature-dependent Young's modulus $E(T)_{\mathrm{PK}}$

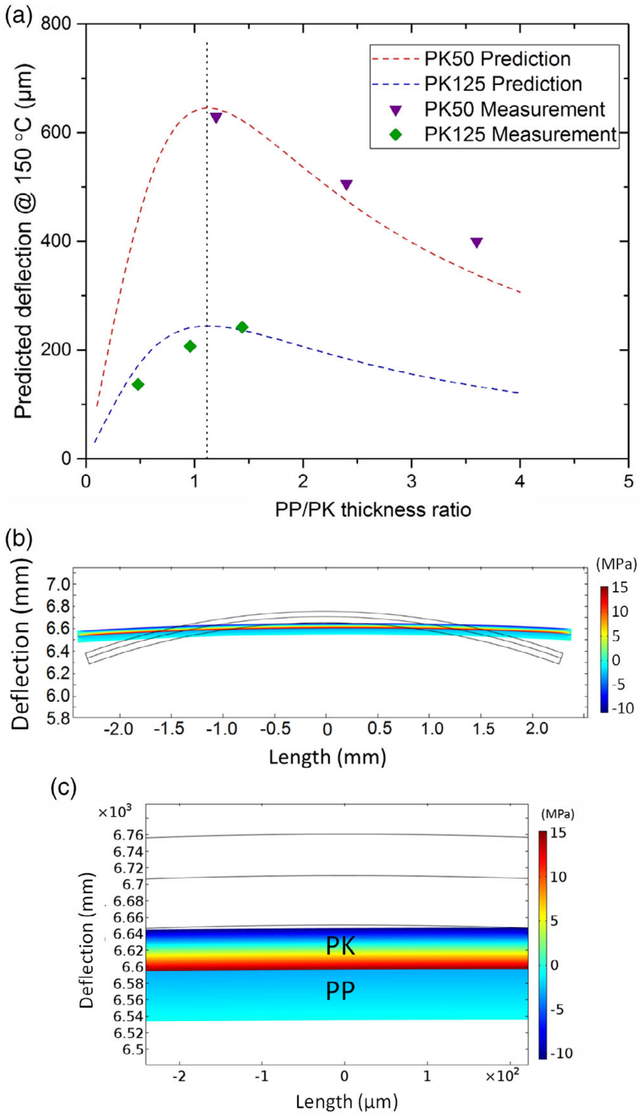

Figure 5. a) Deflection prediction at 150 °C versus PP-to-PK thickness ratio, compared with the measured deflection. The measurements error bars are smaller than ±3 μm. b) The calculated thermal-induced deformation and stress (normal to the x-axis) at 150 °C on a 5 mm-long PK50-PP60 actuator. The original shape is shown as a black outline. c) Zoomed-in view (0.5 mm in length) of the center of the modeled actuator, showing the stress map at 150 °C.

$$E(T)_{\text{PK}} = 3.4 \times 10^{-6} T^4 - 1.8 \times 10^{-3} T^3 + 0.33 T^2 - 30.6 T + 4928 \quad (3)$$

Equation (4) was used for the PP temperature-dependent Young's modulus $E(T)_{\text{PP}}$

$$E(T)_{\text{PP}} = \frac{4.8 \times 10^5}{T^2} + 1.13T + 73 \quad (4)$$

where the young's modulus $E(T)$ is expressed in units of MPa, the temperature T is in units of °C, and the coefficients are rounded to two decimal places.

The actuator was set with a curvature of $R = 6.6$ mm at an initial uniform temperature field of 20 °C. The software was then used to calculate the thermal-induced deformation and induced stress normal to the x-axis at a temperature of 150 °C, where the actuator is expected to be flat. The simulation results shown in Figure 5b display a nearly flat actuator at a temperature of 150 °C, quite similar to the actual measurements. Figure 5b,c also shows the induced stress field due to the deformation at 150 °C. As the PP has a higher CTE than the PK, the PP expands more than the PK during heating, causing tensile stresses in the PK–PP interface area and compressive stresses at the surface of the PK layer. The simulation shows that as the temperature is increased, the PK–PP interface experiences tensile stresses as high as 15 MPa, while the PK experiences compressive stresses of −10 MPa near its surface.

3.5. Applications

A few demonstration devices have been implemeented to show capabilities of the new actuators. To demonstrate the force that a single actuator can apply, a PK125–PP120 actuator weighing 70 mg was placed on a 16 mm support span. A steel nut weighing 30 g was attached to the actuator, as illustrated in **Figure 6**a. When heated by the IR source, the actuator straightened and pulled the steel nut up, thus lifting a weight 428 times of its own. The dashed white line marks the nut base level. The average unbending time during heating was 18 ± 2 s, and the average bending time during cooling was 6 ± 1 s. The full video of weightlifting is available as Video S2, Supporting Information.

To translate the bending motion into a circular motion, an engine was designed. The engine is based on a cogwheel being turned when pushed by the shape change of the 2WSMP actuator. The cogwheel was cut from a 125 μm-thick Kapton film, and the engine body was assembled from BMI 3D-printed parts.

The engine was operated by turning the IR source on and off. When on, the constant power from the IR source heated the actuator until its temperature reached ≈150° and the actuator straightened, pushing the cogwheel clockwise. When the IR source was turned off, the actuator cooled and retracted. The average unbending time during heating was 15 ± 3 s, and the average bending time during cooling was 23 ± 6 s. A Kapton stopper (not shown) at the base of the cogwheel prevented it from turning counterclockwise. With every cycle of heating/cooling, the wheel was turned by several degrees. Figure 6b shows the engine during several cycles of operation. The images show the actuator at both cooled and heated states, and the white dots visualize the wheel rotation. The full video of the engine motion is available as Video S3, Supporting Information.

After experimenting with the 2WSMP-based engine, a miniature vehicle powered by a 2WSMP actuator was built. The vehicle was composed of a front cogwheel, like the one used in the engine, but smaller in diameter, and two back wheels. The vehicle chassis was 3D printed using BMI. A 2WSMP actuator was placed with one end between the back wheels and the other on the cogwheel. A Kapton stopper was placed on a ramp behind the cogwheel to prevent it from turning in the opposite direction.

For the motion test, the IR source was turned on and off sequentially, causing the actuator to straighten and bend, thus

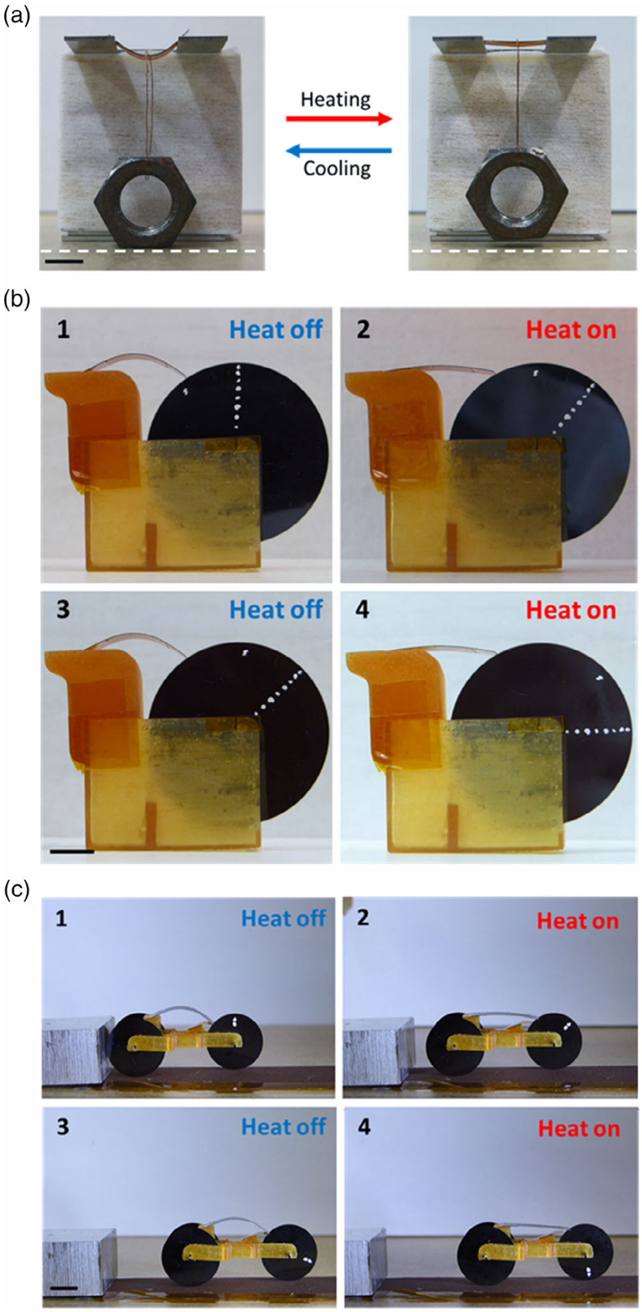

Figure 6. a) A single PK125–PP120 actuator lifting a 30 g weight upon heating by an IR source. b) 2WSMP-based engine at work. The cogwheel is rotated by switching the IR source on and off (the numbers mark the order of frames). c) Summary of the actuator-driven vehicle movement test (the numbers mark the order of frames). Scale bars: 1 cm.

turning the cogwheel and moving the vehicle forward. The average unbending time during heating was 12 ± 2 s, and the average bending time during cooling was 18 ± 3 s. The test was stopped after the front wheel completed half of a cycle, which corresponds to a planar movement of 3 cm. A summary of the movement test is presented in Figure 6c, and the full video is available as Video S4, Supporting Information.

4. Conclusion

Unique 2WSMP bilayer actuators were developed based on PK and PP. While the PK layer provides rigid support, the PP layer is responsible for the deflection of the bilayer due to its higher thermal expansion. The PP maintains its mechanical properties over a wide range of temperatures. This unique combination of properties allowed the development of a series of 2WSMP bilayer actuators that differ by their layer thickness. The effects of the layers' thickness on the reversible shape memory properties and the static forces these 2WSMP bilayers can apply were studied, and their ability to drive a miniature vehicle and engine while remotely activated was demonstrated.

The magnitude of the actuator motion and its accuracy in terms of its repeatability were measured in a series of thermal cycle tests. The results demonstrate that while the PP thickness strongly affects the actuator motion, its repeatability is extremely high regardless of the layers' thickness, suggesting that it can be controlled in the micrometer-scale range. The amount of static force these 2WSMP actuators can apply is proportional to the PP and PK layer thickness. The thickest and strongest actuator tested demonstrated a static force of 1.3 N at 147 °C, equivalent to lifting 6500 times its own weight. The theoretical work at the center point of the 2WSMP actuators is independent of the PK thickness and depends only on the PP layer thickness. Based on Timoshenko's equation, the deflection motion of the 2WSMP actuators was modeled. Fitting of the experimental results to those obtained by the model indicates that thermal expansion variance between the PP and PK layers is the leading mechanism in the reversible shape memory change. The ideal PP/PK thickness ratio, which yields the highest deformation, is 1.1.

The mechanical, thermomechanical, and reversible shape memory properties that were established and proven in this work demonstrate the various possible applications of our 2WSMP bilayers. These properties can be further developed for applications in the field of smart materials, for example, temperature-activated switches, or in the soft robotics field for remotely operated lightweight devices.

Supporting Information

Supporting Information is available from the Wiley Online Library or from the author.

Acknowledgements

The authors would like to thank Dr. Eli Brosh and Michael Amos from Nuclear Research Center Negev and Dr. Davide Levy from Tel-Aviv University for their support with characterization techniques.

Conflict of Interest

The authors declare no conflict of interest.

Data Availability Statement

The data that support the findings of this study are available from the corresponding author upon reasonable request.

Keywords

Kapton, polyPOSS, remote propulsion, reversible shape memory polymers

Received: January 11, 2022
Revised: March 14, 2022
Published online:

[1] T. Liu, T. Zhou, Y. Yao, F. Zhang, L. Liu, Y. Liu, J. Leng, *Composites, Part A* **2017**, *100*, 20.
[2] F. Ge, X. Lu, J. Xiang, X. Tong, Y. Zhao, *Angew. Chem., Int. Ed.* **2017**, *56*, 6126.
[3] T. Ikeda, M. Nakano, Y. Yu, O. Tsutsumi, A. Kanazawa, *Adv. Mater.* **2003**, *15*, 201.
[4] Y. Yu, M. Nakano, A. Shishido, T. Shiono, T. Ikeda, *Chem. Mater.* **2004**, *16*, 1637.
[5] C. J. Barrett, J.-I. Mamiya, K. G. Yager, T. Ikeda, *Soft Matter* **2007**, *3*, 1249.
[6] T. Yoshino, M. Kondo, J.-I. Mamiya, M. Kinoshita, Y. Yu, T. Ikeda, *Adv. Mater.* **2010**, *22*, 1361.
[7] T. Ube, T. Yoda, T. Ikeda, *Liq. Cryst.* **2018**, *45*, 2269.
[8] S. Kobatake, S. Takami, H. Muto, T. Ishikawa, M. Irie, *Nature* **2007**, *446*, 778.
[9] J.-I. Mamiya, A. Kuriyama, N. Yokota, M. Yamada, T. Ikeda, *Chem. Eur. J.* **2015**, *21*, 3174.
[10] H. Finkelmann, E. Nishikawa, G. G. Pereira, M. Warner, *Phys. Rev. Lett.* **2001**, *87*, 015501.
[11] X. Tong, Y. Zhao, *Chem. Mater.* **2009**, *21*, 4047.
[12] Y. Yu, M. Nakano, T. Ikeda, *Nature* **2003**, *425*, 145.
[13] H. Zhang, H. Xia, Y. Zhao, *J. Mater. Chem.* **2012**, *22*, 845.
[14] R. R. Kohlmeyer, M. Lor, J. Chen, *Nano Lett.* **2012**, *12*, 2757.
[15] J. H. Park, B. K. Kim, *Smart Mater. Struct.* **2014**, *23*, 025038.
[16] Y. Liu, J. K. Boyles, J. Genzer, M. D. Dickey, *Soft Matter* **2012**, *8*, 1764.
[17] Y. Shirai, S. Hayashi, *Mitsubishi Tech. Bull. n* **1988**, *184*, 1.
[18] H. Tobushi, S. Hayashi, S. Kojima, *JSME Int J., Ser. 1* **1992**, *35*, 296.
[19] B. K. Kim, S. Y. Lee, M. Xu, *Polymer* **1996**, *37*, 5781.
[20] C. Liang, C. A. Rogers, E. Malafeew, *J. Intell. Mater. Syst. Struct.* **1997**, *8*, 380.
[21] M. Irie, *Shape Mem. Mater.* **1998**, *28*, 203.
[22] A. Lendlein, S. Kelch, *Angew. Chem., Int. Ed.* **2002**, *41*, 2034.
[23] V. A. Beloshenko, V. N. Varyukhin, Y. V. Voznyak, *Russ. Chem. Rev.* **2005**, *74*, 265.
[24] C. Liu, H. Qin, P. T. Mather, *J. Mater. Chem.* **2007**, *17*, 1543.
[25] M. Behl, A. Lendlein, *Mater. Today* **2007**, *10*, 20.
[26] T. Xie, I. A. Rousseau, *Polymer* **2009**, *50*, 1852.
[27] K. Kratz, S. A. Madbouly, W. Wagermaier, A. Lendlein, *Adv. Mater.* **2011**, *23*, 4058.
[28] Q. Zhao, W. Zou, Y. Luo, T. Xie, *Sci. Adv.* **2016**, *2*, e1501297.
[29] T. Chung, A. Romo-Uribe, P. T. Mather, *Macromolecules* **2008**, *41*, 184.
[30] K. M. Lee, P. T. Knight, T. Chung, P. T. Mather, *Macromolecules* **2008**, *41*, 4730.
[31] S. J. Hong, W.-R. Yu, J. H. Youk, *Smart Mater. Struct.* **2010**, *19*, 035022.
[32] K. K. Westbrook, V. Parakh, T. Chung, P. T. Mather, L. C. Wan, M. L. Dunn, H. J. Qi, *J. Eng. Mater. Technol.* **2010**, *132*, 041010.
[33] J. Zotzmann, M. Behl, D. Hofmann, A. Lendlein, *Adv. Mater.* **2010**, *22*, 3424.
[34] J. Li, W. R. Rodgers, T. Xie, *Polymer* **2011**, *52*, 5320.
[35] J.-M. Raquez, S. Vanderstappen, F. Meyer, P. Verge, M. Alexandre, J.-M. Thomassin, C. Jérôme, P. Dubois, *Chem. Eur. J.* **2011**, *17*, 10135.
[36] S. Pandini, S. Passera, M. Messori, K. Paderni, M. Toselli, A. Gianoncelli, E. Bontempi, T. Riccò, *Polymer* **2012**, *53*, 1915.
[37] S. Pandini, F. Baldi, K. Paderni, M. Messori, M. Toselli, F. Pilati, A. Gianoncelli, M. Brisotto, E. Bontempi, T. Riccò, *Polymer* **2013**, *54*, 4253.
[38] A. Lendlein, O. E. C. Gould, *Nat. Rev. Mater.* **2019**, *4*, 116.
[39] M. Behl, K. Kratz, U. Noechel, T. Sauter, A. Lendlein, *Proc. Natl. Acad. Sci. U.S.A.* **2013**, *110*, 12555.
[40] C. Qian, Y. Dong, Y. Zhu, Y. Fu, *Smart Mater. Struct.* **2016**, *25*, 085023.
[41] Y. Gao, W. Liu, S. Zhu, *Macromolecules* **2018**, *51*, 8956.
[42] Y. Gao, W. Liu, S. Zhu, *ACS Appl. Mater. Interfaces* **2017**, *9*, 4882.
[43] M. Behl, K. Kratz, J. Zotzmann, U. Nöchel, A. Lendlein, *Adv. Mater.* **2013**, *25*, 4466.
[44] J. Zhou, S. A. Turner, S. M. Brosnan, Q. Li, J.-M. Y. Carrillo, D. Nykypanchuk, O. Gang, V. S. Ashby, A. V. Dobrynin, S. S. Sheiko, *Macromolecules* **2014**, *47*, 1768.
[45] A. Biswas, V. K. Aswal, P. U. Sastry, D. Rana, P. Maiti, *Macromolecules* **2016**, *49*, 4889.
[46] K. Wang, Y.-G. Jia, X. X. Zhu, *Macromolecules* **2017**, *50*, 8570.
[47] K. K. Westbrook, P. T. Mather, V. Parakh, M. L. Dunn, Q. Ge, B. M. Lee, H. J. Qi, *Smart Mater. Struct.* **2011**, *20*, 065010.
[48] T.-H. Kang, J.-M. Lee, W.-R. Yu, J. H. Youk, H. W. Ryu, *Smart Mater. Struct.* **2012**, *21*, 035028.
[49] S. Chen, J. Hu, H. Zhuo, Y. Zhu, *Mater. Lett.* **2008**, *62*, 4088.
[50] S. Chen, J. Hu, H. Zhuo, *Compos. Sci. Technol.* **2010**, *70*, 1437.
[51] Y. Wu, J. Hu, J. Han, Y. Zhu, H. Huang, J. Li, B. Tang, *J. Mater. Chem. A* **2014**, *2*, 18816.
[52] R. C. P. Verpaalen, T. Engels, A. P. H. J. Schenning, M. G. Debije, *ACS Appl. Mater. Interfaces* **2020**, *12*, 38829.
[53] L. F. Muff, C. Weder, *Adv. Intell. Syst.* **2020**, *2*, 2000177.
[54] A. Miriyev, K. Stack, H. Lipson, *Nat. Commun.* **2017**, *8*, 596.
[55] H. Tamagawa, *Mater. Lett.* **2010**, *64*, 749.
[56] J. Li, Q. Ma, Y. Xu, M. Yang, Q. Wu, F. Wang, P. Sun, *ACS Appl. Mater. Interfaces* **2020**, *12*, 55290.
[57] E. Sachyani, M. Layani, G. Tibi, T. Avidan, A. Degani, S. Magdassi, *Sens. Actuators, B* **2017**, *252*, 1071.
[58] Z. Zeng, H. Jin, L. Zhang, H. Zhang, Z. Chen, F. Gao, Z. Zhang, *Carbon* **2015**, *84*, 327.
[59] L. Chen, M. Weng, Z. Zhou, Y. Zhou, L. Zhang, J. Li, Z. Huang, W. Zhang, C. Liu, S. Fan, *ACS Nano* **2015**, *9*, 12189.
[60] L. Li, J. Meng, C. Hou, Q. Zhang, Y. Li, H. Yu, H. Wang, *ACS Appl. Mater. Interfaces* **2018**, *10*, 15122.
[61] X. Qi, W. Yang, L. Yu, W. Wang, H. Lu, Y. Wu, S. Zhu, Y. Zhu, X. Liu, Y. Dong, Y. Fu, *Polymers* **2019**, *11*, 1599 .
[62] K. Wang, X. X. Zhu, *ACS Biomater. Sci. Eng.* **2018**, *4*, 3099.
[63] Q. Yang, C. Peng, J. Ren, W. Zhao, W. Zheng, C. Zhang, Y. Hu, X. Zhang, *Adv. Opt. Mater.* **2019**, *7*, 1900784.
[64] H.-F. Lu, M. Wang, X.-M. Chen, B.-P. Lin, H. Yang, *J. Am. Chem. Soc.* **2019**, *141*, 14364.
[65] Z. Chen, R. Cao, S. Ye, Y. Ge, Y. Tu, X. Yang, *Sens. Actuators, B* **2018**, *255*, 2971.
[66] A. I. Bram, I. Gouzman, A. Bolker, N. Atar, N. Eliaz, R. Verker, *Nanomaterials* **2022**, *12*, 257.
[67] A. I. Bram, I. Gouzman, A. Bolker, N. Eliaz, R. Verker, *Molecules* **2020**, *25*, 4203.
[68] R. Verker, M. Ozeri, A. Bolker, M. Loeblein, E. H. T. Teo, I. Gouzman, *Polym. Degrad. Stab.* **2016**, *134*, 237.
[69] I. Gouzman, N. Atar, E. Grossman, R. Verker, A. Bolker, M. Pokrass, S. Sultan, O. Sinwani, A. Wagner, T. Lück, C. Seifarth, *Adv. Mater. Technol.* **2019**, *4*, 1900368.
[70] DuPont, *KAPTON Summary of Properties*, https://www.dupont.com/content/dam/dupont/amer/us/en/products/ei-transformation/

documents/EI-10142_Kapton-Summary-of-Properties.pdf (accessed: February 2022).
[71] L. Matějka, A. Strachota, J. Pleštil, P. Whelan, M. Steinhart, M. Šlouf, *Macromolecules* **2004**, *37*, 9449.
[72] Y. Leng, J. Liu, C. Zhang, P. Jiang, *Catal. Sci. Technol.* **2014**, *4*, 997.
[73] S. Bandehali, F. Parvizian, A. Moghadassi, S. M. Hosseini, *Sep. Purif. Technol.* **2020**, *237*, 116361.
[74] S. Timoshenko, *J. Opt. Soc. Am.* **1925**, *11*, 233.
[75] C. Yuan, Z. Ding, T. J. Wang, M. L. Dunn, H. J. Qi, *Smart Mater. Struct.* **2017**, *26*, 105027.
[76] T. van Manen, S. Janbaz, A. A. Zadpoor, *Mater. Today* **2018**, *21*, 144.
[77] R. Verker, N. Atar, F. Quero, S. J. Eichhorn, E. Grossman, *Polym. Degrad. Stab.* **2013**, *98*, 997.
[78] R. Huang, S. Zheng, Z. Liu, T. Y. Ng, *Int. J. Appl. Mech.* **2020**, *12*, 2050014.
[79] G. Stoychev, S. Zakharchenko, S. Turcaud, J. W. C. Dunlop, L. Ionov, *ACS Nano* **2012**, *6*, 3925.

